Experimental Observation of k-Dependent Bulk-Edge Correspondence in Sonic Semimetals with High Winding Numbers

Wei Xiong,[1] Tingde Zhang,[1] Zhiwang Zhang,[1,*] Yuanzhou Zhu,[1] Shuochen Wang,[1] Haixiao Zhang,[1,2] Ying Cheng,[1,3,†] Xiaojun Liu,[1,3,‡] and Johan Christensen[4,§]

[1]*Department of Physics, MOE Key Laboratory of Modern Acoustics, Collaborative Innovation Center of Advanced Microstructures, Jiangsu Physical Science Research Center, Nanjing University, Nanjing 210093, China*

[2]*School of Electrical and Information Engineering, Changzhou Institute of Technology, Changzhou 213032, China*

[3]*State Key Laboratory of Acoustics, Institute of Acoustics, Chinese Academy of Sciences, Beijing 100190, China*

[4]*IMDEA Materials Institute, Calle Eric Kandel, 2, 28906 Getafe, Madrid, Spain*

(Received 23 November 2024; accepted 13 June 2025; published 15 July 2025)

The bulk-edge correspondence plays a crucial role in topological physics bridging the gap between the bulk topology and the topological edge states, which recently was extended to topological metamaterials having a large number of topological boundary states. In this work, we experimentally observe the k-dependent bulk-edge correspondence in the framework of a manmade sonic semimetal, supporting the coexistence of multiple topological phases which are separated by boundaries formed by versatile types of Dirac points. The structure is composed of stacked one-dimensional (1D) extended Su-Schrieffer-Heeger chains through long-range couplings, in which the topological phases are characterized by k-dependent winding numbers. Through an elaborately designed methodology for measuring the acoustic pressure amplitude and phase, we not only derive k-dependent topological winding numbers but also clearly observe the spatial distribution characteristics of edge states across different phases. Our findings significantly broaden the understanding of these critical topological phases and open up avenues for the manipulation of classical waves.

DOI: 10.1103/wkwd-cbn2

Introduction—Exploring exotic topological phases resides at a booming research frontier since the discovery of topological insulators (TIs) and topological semimetals (TSMs) [1–3]. Associated with this, one of the most essential principles is the bulk-edge correspondence [4,5], which bridges the topological protected boundary states with the topology of the bulk. Recent developments in areas such as non-Hermitian TIs [6–13], higher-order TIs [14–16], and non-Abelian physics [17–19] have expanded the concept of the bulk-edge correspondence, providing plenty of unexplored opportunities to unlock the versatility of topological phases. Therefore, detecting topological invariants plays a vital role in characterizing and analyzing a topological system. Another interesting expansion exists in the form of the increment in the bulk invariant and the corresponding numbers of boundary states, which can be traditionally generated through long-range couplings [20–23]. However, both the probing of topological phases and the introduction of long-range couplings meet significant challenges in natural materials.

Thanks to the remarkable possibilities of macroscale artificial structures, manmade symmetry-manipulation for classical waves is readily possible in the study of analogous quantum effects and topological phenomena [24–32]. These customized systems make it easy to fine-tune the versatile geometrical parameters to investigate and validate the vast concepts behind TIs [33–37]. Most recently, variable topological numbers or phases have been realized by incorporating long-range couplings into the artificial topological systems in association with multiple topological interface states in 1D Su-Schrieffer-Heeger (SSH) chain and multiple corner states in two-dimensional (2D) second-order TI [38–41]. Yet, no experimental validation of the large topological index has been reported for TSM. The transitions between multiple topological phases and the rich physics at phase boundaries remain unexplored.

In this work, we discuss a TSM with high winding number, which sustains a pair of type-II semi-Dirac points (SDPs) [42–44] as illustrated in Fig. 1(a). Moreover, we experimentally characterise the associated k-dependent topological indices in an artificial sonic crystal (SC) to verify the inherent bulk-edge correspondence. The TSM is built by stacking the extended 1D SSH chain with long-range couplings between different sublattices. We demonstrate that the topological bulk-edge correspondence in this system can be characterized by the winding number as

*Contact author: zhangzhiwang@nju.edu.cn
†Contact author: chengying@nju.edu.cn
‡Contact author: liuxiaojun@nju.edu.cn
§Contact author: johan.christensen@imdea.org

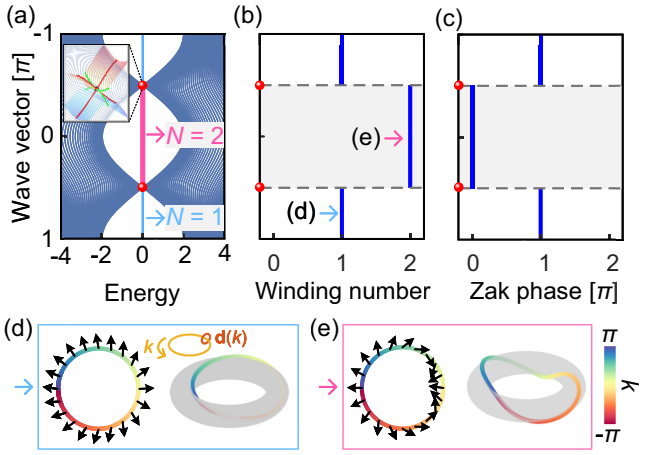

FIG. 1. TSM with type-II SDPs. (a) Projected band diagram, where the blue and red lines represent the topological edge states with $N = 1$ and $N = 2$, respectively, denoting the pair numbers of the zero-energy states. Inset shows the type-II SDP marked by red dots. The k-dependent (b) winding number W and (c) Zak phase. The k-dependent winding numbers of (d) $|W| = 1$ and (e) $|W| = 2$.

shown in Fig. 1(b) instead of the Zak phase in Fig. 1(c), which is zero in the topologically nontrivial region with $N = 2$. Consequently, experimentally measuring the variable winding numbers meets an urgent need. To do so, we design and fabricate a SC composed of waveguide-coupled cavities, and obtain the k-dependent winding numbers from the measured data as outlined in Figs. 1(d) and 1(e) corresponding to $|W| = 1$ and $|W| = 2$, respectively. Furthermore, we successfully detect the momentum-resolved topological edge states and study their energy localization rules in real space, which provide a comprehensive characterization of this unique bulk-edge correspondence.

Tight-binding model—To establish a TSM exhibiting variable k_z-dependent winding numbers, we employ a feasible tight-binding model (TBM) in Fig. 2. Figure 2(a) illustrates the lattice construction by stacking the 1D SSH chain along the z direction, with a and h for the lattice constants. The sublattices A and B are coupled not only through the intralayer nearest-neighbor couplings t_0 and t_1, but also by the intra- and interlayer third-nearest-neighbor couplings t_{2x} and t_{2z} respectively. Under the preservation of chiral symmetry [45], the corresponding Bloch Hamiltonian is given by

$$H(\boldsymbol{k}) = \begin{pmatrix} 0 & Q \\ Q^{\dagger} & 0 \end{pmatrix}, \tag{1}$$

where $Q = t_0 + t_1 e^{-ik_x a} + [t_{2x} + 2t_{2z}\cos(k_z h)]e^{-ik_x 2a}$. By defining $t_2 = t_{2x} + 2t_{2z}\cos(k_z h)$, our 2D TSM can be equivalently represented by a 1D extended SSH model, a concept referred to as dimensional reduction [46–50]. Applying Fourier transformation to the original 2D system yields multiple k_z-dependent 1D systems, with k_z acting as a distinct quantum number. The reduced 1D bulk Hamiltonian is $H_{\text{reduced}}(k_x) = d_x\sigma_x + d_y\sigma_y$, where $\sigma_{x/y}$ denotes the Pauli matrices, and $d_x = t_0 + t_1\cos k_x a + t_2\cos 2k_x a$, $d_y = t_1\sin k_x a + t_2\sin 2k_x a$. The winding number, derived from the trace of $\mathbf{d}(k_x)$ as k_x varies from $-\pi$ to π, characterizes this 1D chiral-symmetric system. Figure 2(b) illustrates the phase diagram, showing the absolute value of the winding number $|W|$ as a function of t_1/t_0 and t_2/t_0. It reveals three distinct regions defined by specific quantized topological invariants, which are separated by phase boundaries in form of Dirac points or type-II SDPs in 2D TSM. Inside each region, terminal traces of the vector $\mathbf{d}(k_x)$ on the (d_x, d_y) plane are depicted, with red points denoting the origin. For instance, within the red area, the terminal trace forms a closed loop encircling the origin twice, indicating a bulk winding number of $|W| = 2$. We demonstrate that the orientation of the loop signifies the sign of the winding number, but only the absolute value matters in this work. The opposite sign leads to the distinct rules for the field distributions of edge states (see Supplemental Material Sec. I [51]). Figure 2(c) depicts a specific trajectory as indicated by the green line in Fig. 2(b), showing the progression while increasing t_2/t_0 but maintaining $t_1/t_0 = 2$ constant. Notably, it unveils the bulk gap closure at $t_2/t_0 = 1$ and -3, consistent with the phase transition criterion of $|t_1| = |t_0 + t_2|$. Because of the impact of k_z on the value of t_2, the parameter t_2/t_0 traces a circular route as k_z sweeping from $-\pi/h$ to π/h in the phase diagram slice shown in Fig. 2(c), which is centered at t_{2x} with a radius of $2|t_{2z}|$. With different centers and radii, i.e., different couplings, the stacked 2D model could span a wide range of topological phases, encompassing trivial insulators, TIs, and TSMs (see Supplemental Material Sec. II [51]).

An illustrative example of a TSM with k-dependent winding numbers is established with $t_{2x} = 2$ and $t_{2z} = 1$, of which the variation of the topological phase exactly obeys the route shown in Fig. 2(c), passing through two regions with different winding numbers. From the calculated band diagram in Fig. 2(d) and the topological winding numbers in Fig. 2(e), we can clearly observe the topological phase transition at a pair of type-II SDPs with $(k_x, k_z) = (\pm\pi/a, \pm k_D)$. The proposed type-II SDP features a linear dispersion along k_z direction but a quadratic relation along k_x direction, which forms a crescent shape, and can be viewed as the merging of three Dirac points (see Supplemental Material Sec. III [51] and video I). The calculated winding number for $|k_z| > k_D$ equals to 1 and that for $|k_z| < k_D$ is 2, indicating the presence of topological edge states with the variable numbers following the bulk-edge correspondence. To observe it, we employ a ribbonlike supercell as shown in Fig. 2(f), of which the projected dispersion relations are plotted in Fig. 2(g). One pair of the degenerate edge states (ES I) is found within

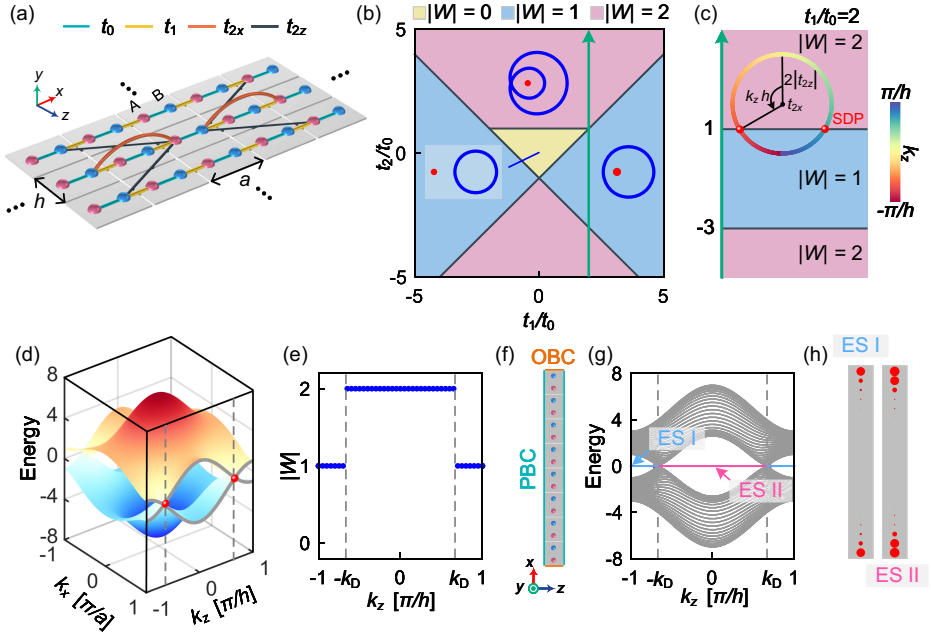

FIG. 2. Bulk-edge correspondence in TBM. (a) Schematic of the proposed 2D TSM. The long-range couplings (t_{2x}/t_{2z}) connected with the central unit cell are plot while others not shown here for simplicity. (b) Topological phase diagram for the reduced 1D system. Yellow, blue, and red colored regions represent the situations with the winding number of 0, 1, and 2, respectively. (c) A slice of the phase diagram for $t_1/t_0 = 2$ as labeled by the green line in (b). (d) Band diagrams related to k_x and k_z. The slice with $k_x = \pi/a$ is highlighted by gray curves where the red globules mark the type-II SDPs. (e) Calculated k_z-dependent winding numbers $|W|$. (f) Schematic and (g) projected dispersion relations of a supercell which is periodic along z direction but finite along the x axis. (h) Eigenfunctions of ES I and ES II as labeled in (g).

$|k_z| > k_D$ (labeled by blue lines), and the numbers of the edge states are doubled within $|k_z| < k_D$ (ES II labeled by red lines). Furthermore, Fig. 2(h) illustrates typical eigenfield distributions of ES I and ES II for $k_z = -\pi/h$ and $k_z = 0$, respectively. We demonstrate that the eigenfunctions of ES I with $|W| = 1$ are highly localized at the outermost sites with exponential decay into bulk, but those of ES II with $|W| = 2$ are confined at the first two unit cells. We also want to emphasize that the maximum winding number in an extended SSH model, in which the long-range couplings connect the unit cell with its mth nearest neighbor ones, is m. Simultaneously, the corresponding zero-energy topological edge states are predominantly confined within the first m unit cells at each boundary, and type-II SDPs still persist while increasing m (see Supplemental Material Sec. IV [51]).

Acoustic realization—Next, we design an acoustic cavity-tube framework to construct the above-studied TBM. The first-order resonant mode of the sound cavity functions as the on-site orbital and interconnecting tubes emulate the coupling interactions. Through meticulously engineering the length and cross-sectional area of these coupling tubes, we can attain the desired coupling strength and maintain the chiral symmetry [55,56] in the system (see Supplemental Material Sec. V [51]). Figure 3(a) illustrates the assembling process of the designed SC, and details can be found in End Matter. The projected dispersions of a ribbonlike supercell acquired through the finite-element method (FEM) [dots in Fig. 3(b)] demonstrate great agreement with the outcomes from the TBM (colored curves). As anticipated, SDPs appear at $k_z = \pm k_D$ and are fixed at $f_0 = 5720$ Hz. As shown in the inset, the winding number $|W|$ exhibits nontrivial phases in the gapped momentum space with distinct values of $|W| = 1$ for $|k_z| < k_D$ and $|W| = 2$ for $|k_z| > k_D$. According to the bulk-edge correspondence, two types of topological edge stats denoted as ES I and ES II link the SDPs but with the different numbers of states. To prove it, Figs. 3(c) and 3(d) present the calculated eigenspectra at $k_z = 0$ and $k_z = \pi/h$, respectively. Notably, one pair of edge states arises in the band gap at $k_z = 0$ and there are two pairs of edge states at $k_z = \pi/h$ for comparison due to the doubling of the winding number. Besides the different numbers of states, the spatial field distributions of ES I and ES II also display differences, as evident from the pressure distributions shown in Figs. 3(e) and 3(f). One can observe that most of the energy for ES I is localized at the terminal sites [1 and 40 in Fig. 3(e)], but sounds for ES II can be also trapped at the neighboring unit cells adjacent to the terminal ones [sites 1, 3, 38 and 40 in Fig. 3(f)], agreeing well with the TBM predictions. These unique spatial characteristics provide possibilities for distinguishing the topological edge states with different winding numbers in experiments. Analysis on other topological phases using the proposed acoustic cavity-tube

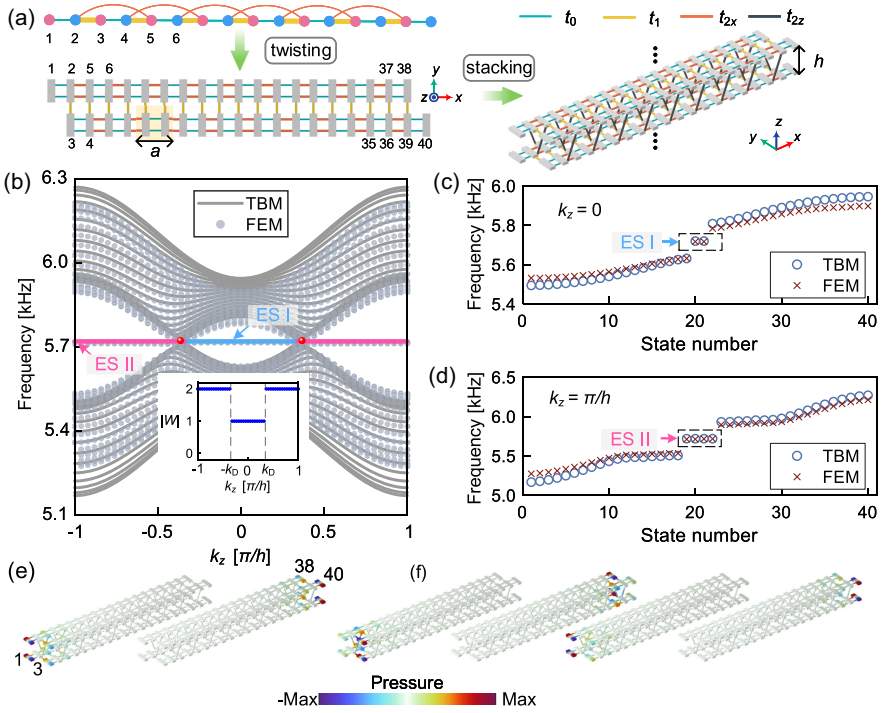

FIG. 3. Realization of acoustic TSM with k_z-dependent winding number. (a) Flow schematic of designing the acoustic TSM through twisting and stacking waveguide-coupled cavities. (b) Edge-projected dispersions calculated for the semi-infinite SC which is infinite along z direction but finite along x axis. Inset shows the winding number for different k_z. Eigenfrequency spectra for (c) $k_z = 0$ and (d) $k_z = \pi/h$. Acoustic eigenfield profiles of (e) one pair of topological edge states with $k_z = 0$ and (f) two pairs of topological edge states with $k_z = \pi/h$.

framework can be found in Supplemental Material Sec. VI [51].

Experimental measurements—To validate this unique k-dependent bulk-edge correspondence, we 3D print a finite SC as depicted in Fig. 4(a), which consists of 12 layers along z direction with 22 unit cells in each layer. By performing 2D Fourier transform on the detected signals through leveraging the twice-excitation pump-probe approach (see Supplemental Material Sec. VII [51]), the bulk band diagrams with different k_z slices are achieved as

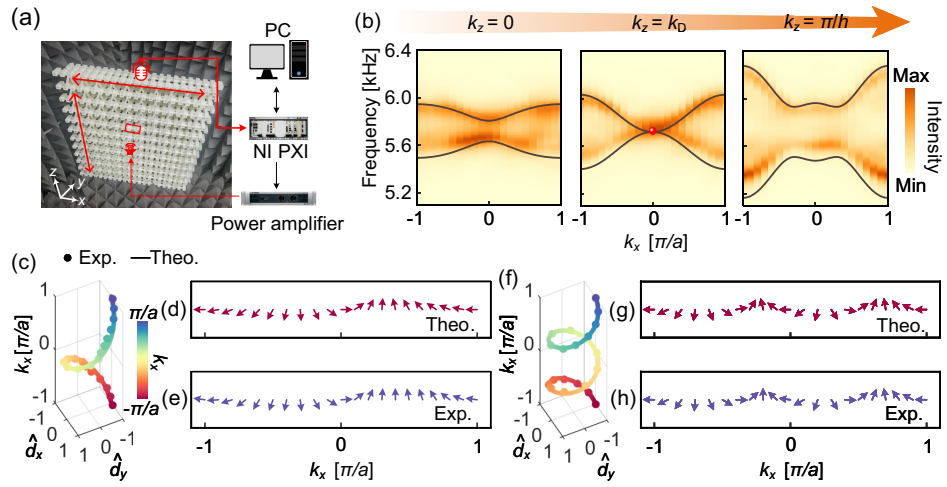

FIG. 4. Experimentally measuring the k_z-dependent winding numbers. (a) Photo of the printed SC and the experimental setup. (b) Measured band structures (background color map) at different k_z while scanning k_x together with the TBM results (black curves) for comparison. (c) Theoretically derived and experimentally measured evolution of $\hat{d}_x$ and $\hat{d}_x$ with $k_z h = 0$. The corresponding evolution of the vector $\hat{\mathbf{d}}(k_x)$ is also shown by the arrows via (d) theory and (e) experiments. (f)–(h) Same as (c)–(e), but for $k_z = \pi/h$.

shown by the background colors in Fig. 4(b), showing a close agreement with the TBM results. The whole band diagrams in $k_x - k_z$ plane can be found in Supplemental Material Sec. VIII [51]. The measured band broadening is attributed to the inevitable viscous loss in experiments. At $k_z = 0$, a band gap exists near f_0 and becomes smaller while increasing k_z. A SDP appears when $k_z = k_D$ as a hallmark feature of the TSM and the parabolic dispersion along k_x can be clearly observed. Further increasing k_z leads to the reopening of the band gap and topological phase transition occurs. To verify this phase transition, we experimentally measure the topological invariants, indicating the distinctive bulk topology of the TSM under different k_z. Utilizing singular value decomposition of the measured response tensor, which could mitigate the inevitable noise induced by the measured nontarget eigenstates, we extract precise wave functions $u_{n,\boldsymbol{k}}$ and derive the Bloch matrix $H(\boldsymbol{k})$ as

$$H(\boldsymbol{k}) = R(\boldsymbol{k}) \begin{bmatrix} E_1(\boldsymbol{k}) & 0 \\ 0 & E_2(\boldsymbol{k}) \end{bmatrix} R(\boldsymbol{k})^T$$
$$R(\boldsymbol{k}) = [u_1(\boldsymbol{k})\, u_2(\boldsymbol{k})] \in \mathrm{O}(2). \quad (2)$$

Subsequently, for the chosen k_z, the normalized $\mathbf{d}(k_x)$ $[\hat{\mathbf{d}}(k_x)]$ is extracted from $H(\boldsymbol{k})$ to track its trajectory as k_x spans from $-\pi/a$ to π/a. Figure 4(c) describes this trajectory with $k_z = 0$ via both theory (curve) and experiment (dots), presenting perfect consistency. The vector $\hat{\mathbf{d}}(k_x)$ completes one cycle around the origin indicating the winding number of $|W| = 1$. To make it more transparent, we plot the theoretical and measured $\hat{\mathbf{d}}(k_x)$ for each k_x in Figs. 4(d) and 4(e), respectively. While for the case with $k_z = \pi/h$ in Figs. 4(f)–4(h), the trajectory of $\hat{\mathbf{d}}(k_x)$ experiences two cycles and thus demonstrates the winding number of $|W| = 2$. These measurements provide compelling evidence for the topological phase transition happened at SDP. Note that our model is characterized by a unique combination of various topological nontrivial phases, setting it apart from previous TSMs featuring one trivial and the other nontrivial phases [48,49]. We want to emphasize that the above-discussed methodology gives rise to universal applicability and could be extended to diverse physical systems for precisely detecting their topological invariants (see Supplemental Material Sec. VII [51]).

Finally, we focus on the experimental measurements of the topological edge states, of which the number differs for $|k_z| > k_D$ and $|k_z| < k_D$ due to their different winding numbers. To provide a deeper understanding of this unique bulk-edge correspondence in experiment, we perform a pump-probe method while placing a loudspeaker at the specific edge site of the middle layer (the 6th layer). Then the pressure fields are recorded from the cavities which are located at the same sites as the source but in the different layers along the vertical z direction (see Supplemental Material Secs. IX and X [51]). Figure 5(a) shows the measured projected edge dispersions after performing 1D Fourier transformation with the source placed at site 1 (red star in the inset) of the 6th layer. The edge states are clearly visible across the whole momentum space and agree well with the theoretical outcomes (curves). To illustrate the spatial characteristics of the edge states, we further analyze the response signals from all of the cavities. As shown in Fig. 5(b), we fix the input frequency as $f_0 = 5720$ Hz and Fourier transform z into k_z at each site, showcasing a dependence on both wave vector and site positions. The edge states are prominently excited for all k_z, as both ES I and ES II are localized at site 1. Additionally, Fig. 5(c) provides further verifications through the spatial pressure distributions by setting $k_z = 0$ (orange) and π/h (green). For comparison, a similar experimental procedure is adopted with the source placed at site 3 as labeled in the inset of Fig. 5(d). From the experimental data, we find that the peaks for ES I vanish within $|k_z| < k_D$, because it is localized solely at site 1 and thus cannot be well excited when source is placed at site 3. In contrast, for $|k_z| > k_D$,

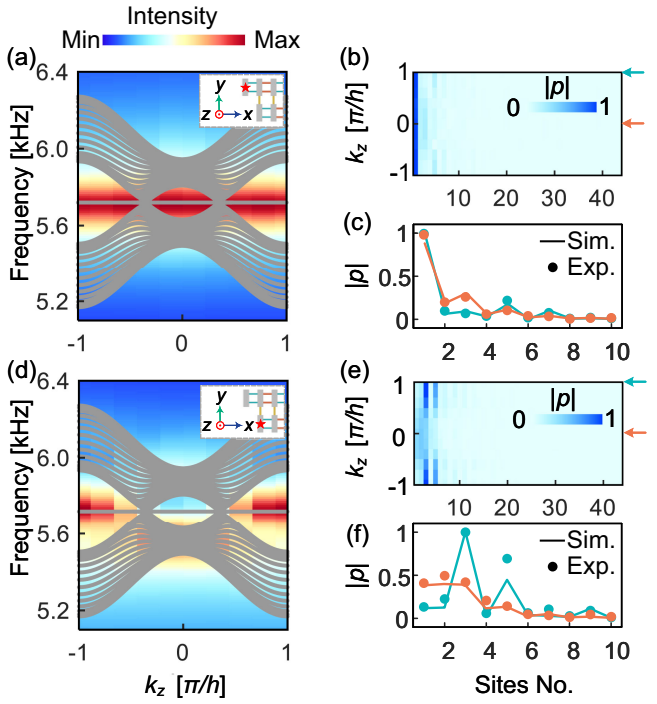

FIG. 5. Experimental observations of the k_z-dependent topological edge states. (a) Measured (color map) edge-projected dispersions along k_z when a point source is placed at the site-1 cavity as shown in inset. (b) Measured distributions of the pressure amplitudes after Fourier transforming the sound fields at each column of cavities along z direction. The site numbers have been labeled in Fig. 3(a). (c) Simulated (lines) and experimentally measured (dots) distributions of the pressure amplitudes at two specific k_z values of 0 and π/h. (d)–(f) Same as (a)–(c) but the point source is placed at the site-3 cavity of one layer near the sample center.

the ES II can be still clearly observed, which could be also confirmed by Figs. 5(e) and 5(f). These measurements exhibit excellent agreements with FEM simulations when the inherent viscous losses are taken into account (see Supplemental Material Sec. IX [51]).

Conclusions—In conclusion, we have proposed a 2D TSM which obeys the unique bulk-edge correspondence characterized by the k-dependent winding numbers. The modulations on the intra- and interlayer couplings induce the emergence of the large topological invariant. Specifically, we build a TSM by stacking the twisted acoustic SSH chain, which supports a pair of SDPs and the variation of the topological winding numbers from 1 to 2. Through the precisely designed experiments, we not only successfully detect such k-dependent topological indices, but also experimentally observe the spatial distribution properties of the topological edge states, which establish a complete and comprehensive understanding of the bulk-edge correspondence. We demonstrate that the topological edge states in the proposed TSM, dependent on both real and reciprocal spaces, may provide potential applications in guiding, sensing, and splitting for classical waves [57–59].

Acknowledgments—This work was supported by the National Key R&D Program of China (2022YFA1404501 and 2022YFA1404400), NSFC (12074183, 12227809, 12225408, 12474439 and 12474448), and the Natural Science Foundation of Jiangsu Province (BK20240061 and BK20233001). J. C. acknowledges support from the Spanish Ministry of Science and Innovation through a Consolidación Investigadora Grant (CNS2022-135706). We thank Z.-K. Lin of The University of Hong Kong for helpful discussions.

Data availability—The data supporting this study's findings are available within the Letter.

[1] M. Z. Hasan and C. L. Kane, Colloquium: Topological insulators, Rev. Mod. Phys. **82**, 3045 (2010).
[2] X.-L. Qi and S.-C. Zhang, Topological insulators and superconductors, Rev. Mod. Phys. **83**, 1057 (2011).
[3] J. E. Moore, The birth of topological insulators, Nature (London) **464**, 194 (2010).
[4] Y. Hatsugai, Chern number and edge states in the integer quantum Hall effect, Phys. Rev. Lett. **71**, 3697 (1993).
[5] E. Prodan and H. Schulz-Baldes, *Bulk and Boundary Invariants for Complex Topological Insulators*, Mathematical Physics Studies (Springer, Cham, 2016).
[6] F. K. Kunst, E. Edvardsson, J. C. Budich, and E. J. Bergholtz, Biorthogonal bulk-boundary correspondence in non-Hermitian systems, Phys. Rev. Lett. **121**, 026808 (2018).
[7] Z. Gong, Y. Ashida, K. Kawabata, K. Takasan, S. Higashikawa, and M. Ueda, Topological phases of non-Hermitian systems, Phys. Rev. X **8**, 031079 (2018).
[8] K. Kawabata, K. Shiozaki, M. Ueda, and M. Sato, Symmetry and topology in non-Hermitian physics, Phys. Rev. X **9**, 041015 (2019).
[9] A. Ghatak, M. Brandenbourger, J. Van Wezel, and C. Coulais, Observation of non-Hermitian topology and its bulk–edge correspondence in an active mechanical metamaterial, Proc. Natl. Acad. Sci. U.S.A. **117**, 29561 (2020).
[10] Z. Yang, K. Zhang, C. Fang, and J. Hu, Non-Hermitian bulk-boundary correspondence and auxiliary generalized Brillouin zone theory, Phys. Rev. Lett. **125**, 226402 (2020).
[11] L. Xiao, T. Deng, K. Wang, G. Zhu, Z. Wang, W. Yi, and P. Xue, Non-Hermitian bulk-boundary correspondence in quantum dynamics, Nat. Phys. **16**, 761 (2020).
[12] T. Helbig, T. Hofmann, S. Imhof, M. Abdelghany, T. Kiessling, L. Molenkamp, C. Lee, A. Szameit, M. Greiter, and R. Thomale, Generalized bulk–boundary correspondence in non-Hermitian topolectrical circuits, Nat. Phys. **16**, 747 (2020).
[13] F. Schindler, K. Gu, B. Lian, and K. Kawabata, Hermitian bulk–non-Hermitian boundary correspondence, PRX Quantum **4**, 030315 (2023).
[14] W. A. Benalcazar, B. A. Bernevig, and T. L. Hughes, Electric multipole moments, topological multipole moment pumping, and chiral hinge states in crystalline insulators, Phys. Rev. B **96**, 245115 (2017).
[15] W. A. Benalcazar, B. A. Bernevig, and T. L. Hughes, Quantized electric multipole insulators, Science **357**, 61 (2017).
[16] W. A. Benalcazar, T. Li, and T. L. Hughes, Quantization of fractional corner charge in C_n-symmetric higher-order topological crystalline insulators, Phys. Rev. B **99**, 245151 (2019).
[17] Q. Wu, A. A. Soluyanov, and T. Bzdušek, Non-Abelian band topology in noninteracting metals, Science **365**, 1273 (2019).
[18] A. Bouhon, Q. Wu, R.-J. Slager, H. Weng, O. Yazyev, V, and T. Bzdusek, Non-Abelian reciprocal braiding of Weyl points and its manifestation in ZrTe, Nat. Phys. **16**, 1137 (2020).
[19] A. Tiwari and T. c. v. Bzdušek, Non-Abelian topology of nodal-line rings in $\mathcal{PT}$-symmetric systems, Phys. Rev. B **101**, 195130 (2020).
[20] D. Sticlet and F. Piéchon, Distant-neighbor hopping in graphene and Haldane models, Phys. Rev. B **87**, 115402 (2013).
[21] D. Sticlet, F. Piéchon, J.-N. Fuchs, P. Kalugin, and P. Simon, Geometrical engineering of a two-band Chern insulator in two dimensions with arbitrary topological index, Phys. Rev. B **85**, 165456 (2012).
[22] L. Lin, Y. Ke, and C. Lee, Real-space representation of the winding number for a one-dimensional chiral-symmetric topological insulator, Phys. Rev. B **103**, 224208 (2021).
[23] W. A. Benalcazar and A. Cerjan, Chiral-symmetric higher-order topological phases of matter, Phys. Rev. Lett. **128**, 127601 (2022).
[24] Z. Wang, Y. Chong, J. D. Joannopoulos, and M. Soljačić, Observation of unidirectional backscattering-immune topological electromagnetic states, Nature (London) **461**, 772 (2009).

[25] Y. Poo, R.-X. Wu, Z. Lin, Y. Yang, and C. T. Chan, Experimental realization of self-guiding unidirectional electromagnetic edge states, Phys. Rev. Lett. **106**, 093903 (2011).
[26] R. Süsstrunk and S. D. Huber, Observation of phononic helical edge states in a mechanical topological insulator, Science **349**, 47 (2015).
[27] L. Lu, L. Fu, J. D. Joannopoulos, and M. Soljačić, Weyl points and line nodes in gyroid photonic crystals, Nat. Photonics **7**, 294 (2013).
[28] L. Lu, Z. Wang, D. Ye, L. Ran, L. Fu, J. D. Joannopoulos, and M. Soljačić, Experimental observation of Weyl points, Science **349**, 622 (2015).
[29] M. Xiao, W.-J. Chen, W.-Y. He, and C. T. Chan, Synthetic gauge flux and Weyl points in acoustic systems, Nat. Phys. **11**, 920 (2015).
[30] Z. Yang and B. Zhang, Acoustic type-II Weyl nodes from stacking dimerized chains, Phys. Rev. Lett. **117**, 224301 (2016).
[31] F. Li, X. Huang, J. Lu, J. Ma, and Z. Liu, Weyl points and Fermi arcs in a chiral phononic crystal, Nat. Phys. **14**, 30 (2018).
[32] H. He, C. Qiu, L. Ye, X. Cai, X. Fan, M. Ke, F. Zhang, and Z. Liu, Topological negative refraction of surface acoustic waves in a Weyl phononic crystal, Nature (London) **560**, 61 (2018).
[33] T. Li, L. Liu, Q. Zhang, and C. Qiu, Acoustic realization of projective mirror Chern insulators, Commun. Phys. **6**, 268 (2023).
[34] Z.-K. Lin, Y. Zhou, B. Jiang, B.-Q. Wu, L.-M. Chen, X.-Y. Liu, L.-W. Wang, P. Ye, and J.-H. Jiang, Measuring entanglement entropy and topological signature for phononic systems, Nat. Commun. **15**, 1601 (2024).
[35] K. Wang, A. Dutt, K. Y. Yang, C. C. Wojcik, J. Vučković, and S. Fan, Generating arbitrary topological windings of a non-Hermitian band, Science **371**, 1240 (2021).
[36] V. Peri, Z.-D. Song, M. Serra-Garcia, P. Engeler, R. Queiroz, X. Huang, W. Deng, Z. Liu, B. A. Bernevig, and S. D. Huber, Experimental characterization of fragile topology in an acoustic metamaterial, Science **367**, 797 (2020).
[37] G. Li, L. Wang, R. Ye, Y. Zheng, D.-W. Wang, X.-J. Liu, A. Dutt, L. Yuan, and X. Chen, Direct extraction of topological Zak phase with the synthetic dimension, Light Sci. Appl. **12**, 81 (2023).
[38] H. Liu, X. Huang, M. Yan, J. Lu, W. Deng, and Z. Liu, Acoustic topological metamaterials of large winding number, Phys. Rev. Appl. **19**, 054028 (2023).
[39] D. Wang, Y. Deng, J. Ji, M. Oudich, W. A. Benalcazar, G. Ma, and Y. Jing, Realization of a Z-classified chiral-symmetric higher-order topological insulator in a coupling-inverted acoustic crystal, Phys. Rev. Lett. **131**, 157201 (2023).
[40] Y. Li, H. Qiu, Q. Zhang, and C. Qiu, Acoustic higher-order topological insulators protected by multipole chiral numbers, Phys. Rev. B **108**, 205135 (2023).
[41] F. Pellerin, R. Houvenaghel, W. A. Coish, I. Carusotto, and P. St-Jean, Wave-function tomography of topological dimer chains with long-range couplings, Phys. Rev. Lett. **132**, 183802 (2024).
[42] J. Wang, S. Deng, Z. Liu, and Z. Liu, The rare two-dimensional materials with Dirac cones, Natl. Sci. Rev. **2**, 22 (2015).
[43] H. Huang, Z. Liu, H. Zhang, W. Duan, and D. Vanderbilt, Emergence of a Chern-insulating state from a semi-Chern dispersion, Phys. Rev. B **92**, 161115(R) (2015).
[44] Y. Shao, S. Moon, A. N. Rudenko, J. Wang, J. Herzog-Arbeitman, M. Ozerov, D. Graf, Z. Sun, R. Queiroz, S. H. Lee, Y. Zhu, Z. Mao, M. I. Katsnelson, B. A. Bernevig, D. Smirnov, A. J. Millis, and D. N. Basov, Semi-Dirac fermions in a topological metal, Phys. Rev. X **14**, 041057 (2024).
[45] C.-K. Chiu, J. C. Y. Teo, A. P. Schnyder, and S. Ryu, Classification of topological quantum matter with symmetries, Rev. Mod. Phys. **88**, 035005 (2016).
[46] X.-L. Qi, T. L. Hughes, and S.-C. Zhang, Topological field theory of time-reversal invariant insulators, Phys. Rev. B **78**, 195424 (2008).
[47] Z.-K. Lin, Y. Wu, B. Jiang, Y. Liu, S.-Q. Wu, F. Li, and J.-H. Jiang, Topological Wannier cycles induced by sub-unit-cell artificial gauge flux in a sonic crystal, Nat. Mater. **21**, 430 (2022).
[48] Q. Wei, X. Zhang, W. Deng, J. Lu, X. Huang, M. Yan, G. Chen, Z. Liu, and S. Jia, Higher-order topological semimetal in acoustic crystals, Nat. Mater. **20**, 812 (2021).
[49] H. Qiu, M. Xiao, F. Zhang, and C. Qiu, Higher-order Dirac sonic crystals, Phys. Rev. Lett. **127**, 146601 (2021).
[50] H. Qiu, Y. Li, Q. Zhang, and C. Qiu, Discovery of higher-order nodal surface semimetals, Phys. Rev. Lett. **132**, 186601 (2024).
[51] See Supplemental Material at http://link.aps.org/supplemental/10.1103/wkwd-cbn2 for (I) TSM hosting opposite winding numbers, (II) versatile topological phases predicted by the TBM, (III) properties of type-II semi-Dirac point, (IV) TSM hosting larger winding numbers, (V) geometric details of SC, (VI) versatile topological phases achieved by acoustic structure, (VII) measuring dispersions and wave functions, (VIII) whole band structure of the designed sonic crystal, (IX) simulation results of the k_z-dependent topological edge states, and (X) numerical and experimental methods. Supplemental video I shows the process of merging three Dirac points into a type-II SDP. The Supplemental Material also contains Refs. [52–54].
[52] M. Milićević, G. Montambaux, T. Ozawa, O. Jamadi, B. Real, I. Sagnes, A. Lemaître, L. Le Gratiet, A. Harouri, J. Bloch, and A. Amo, Type-III and tilted Dirac cones emerging from flat bands in photonic orbital graphene, Phys. Rev. X **9**, 031010 (2019).
[53] P. Dietl, F. Piéchon, and G. Montambaux, New magnetic field dependence of Landau levels in a graphenelike structure, Phys. Rev. Lett. **100**, 236405 (2008).
[54] W. Wang, Z.-G. Chen, and G. Ma, Synthetic three-dimensional $\mathbb{Z} \times \mathbb{Z}_2$ topological insulator in an elastic metacrystal, Phys. Rev. Lett. **127**, 214302 (2021).
[55] Z.-G. Chen, L. Wang, G. Zhang, and G. Ma, Chiral symmetry breaking of tight-binding models in coupled acoustic-cavity systems, Phys. Rev. Appl. **14**, 024023 (2020).
[56] Y. Deng, W. A. Benalcazar, Z.-G. Chen, M. Oudich, G. Ma, and Y. Jing, Observation of degenerate zero-energy

topological states at disclinations in an acoustic lattice, Phys. Rev. Lett. **128**, 174301 (2022).
[57] W. Zhao, Y. Zheng, C. Lu, Z. Wang, Y.-C. Liu, and S. Zhang, Landau rainbow induced by artificial gauge fields, Phys. Rev. Lett. **133**, 233801 (2024).
[58] B. Hu, Z. Zhang, H. Zhang, L. Zheng, W. Xiong, Z. Yue, X. Wang, J. Xu, Y. Cheng, X. Liu *et al.*, Non-Hermitian topological whispering gallery, Nature (London) **597**, 655 (2021).
[59] X. Zhang, F. Zangeneh-Nejad, Z. G. Chen, M. Lu, and J. Christensen, A second wave of topological phenomena in photonics and acoustics, Nature (London) **618**, 687 (2023).

End Matter

Appendix A: Assembling process of the designed SC—As shown in Fig. 3(a), the 1D extended SSH chain along x axis is first twisted towards a double-array chain to achieve the long-range coupling strength, like t_{2x} between sites 2 and 5. Then, the structure is stacked along the z direction to create the TSM and each single layer is connected by the long-range coupling t_{2z}. The lattice constants along x and z directions are designated as $a = 27.7$ and $h = 9.6$ mm, respectively. We highlight that the proposed construction methodology offers significant design flexibility, enabling the realization of complex theoretical models characterized by intricate long-range couplings.